Soft Matter

Cite this: *Soft Matter*, 2012, **8**, 12124

www.rsc.org/softmatter

PAPER

Lyotropic phase behavior of polymer-coated iron oxide nanoparticles†

Sara Mehdizadeh Taheri,*[a] Steffen Fischer,[a] Martin Trebbin,[a] Sebastian With,[a] Jan H. Schröder,[a] Jan Perlich,[b] Stephan V. Roth[b] and Stephan Förster[a]

Received 1st August 2012, Accepted 18th September 2012
DOI: 10.1039/c2sm26777b

We show that monodisperse iron oxide nanoparticles in the size range of 6–17 nm, coated with brush-like layers of polystyrene or polyisoprene of different molecular weights, form well-defined lyotropic liquid crystalline phases. The lyotropic phase behaviour was investigated by synchrotron small-angle X-ray scattering. With increasing concentration, the polymer-coated nanoparticles show a disorder–order transition into well ordered bcc- or fcc-phases, depending on nanoparticle size and polymer molecular weights. The lyotropic phases can be shear oriented to obtain macroscopic highly ordered single crystalline nanoparticle superlattices exhibiting more than 100 Bragg-peaks. Within the ordered phases, the distance between adjacent nanoparticles can be varied systematically *via* concentration and attached polymer molecular weights in a range of 10–40 nm. We further demonstrate the versatility of lithographically patterned microstructured sample holders in combination with microfocus X-ray beams, which allow the investigation of very small sample volumes.

Introduction

The spontaneous assembly to form ordered crystalline phases is a well-known property of colloidal particles. Common examples comprise dispersion colloids such as polymer latices, silica particles or microgels, as well as association colloids such as surfactant and polymer micelles. Of particular current interest are colloidal particles that form ordered phases in solution, *i.e.* in the lyotropic state, because established wet-chemical processes such as sol–gel-chemistry or polymerization reactions can be used to transform them into solid ordered materials that would otherwise be very difficult or impossible to prepare. The most prominent example is their use as templates to generate photonic crystals.

For many applications, it would be desirable to similarly assemble nanoparticles into lyotropic colloidal crystals. The formation of ordered crystalline assemblies of nanoparticles was quickly reported after synthetic methods to generate nanoparticles with sufficiently narrow size distributions had been established.[1] Since then, there have been many reports of superlattice formation for different nanoparticles and also binary nanoparticle mixtures,[2] mostly in the form of monolayers or micron-size crystals.[3] These assemblies are mostly produced *via* drop casting on solid supports, or by controlled crystallization from dilute solutions.[4]

In most cases of ordered nanoparticle assembly, a control over the interparticle distance was neither possible nor intended. For conventional nanoparticle assemblies, some control of the interparticle distance is possible *via* the choice of the stabilizing surfactants that can differ in the length of their alkyl chains.[5] A breakthrough has been the use of DNA-ligands by Alivisatos and Mirkin *et al.*,[6–8] who for gold nanoparticles tailored the superlattice type and nanoparticle distance *via* hybridization of DNA-chains. If the DNA-chains were not hybridizing, lyotropic phases of cubic symmetry were formed. The lyotropic phase behaviour could be followed by microfocus synchrotron X-ray scattering of a small droplet of a DNA-coated gold nanoparticle aqueous solution upon drying.[9,10]

Since the DNA@Au system builds upon the unique and stable Au–S–DNA end group attachment and has its limitations in the amount of material that can be produced, it would be highly desirable to have more versatile and upscalable polymer@-nanoparticle systems. We have recently developed a method to attach polymer chains with their chain end to nanoparticles *via* a ligand exchange procedure.[11,12] It builds upon the advantages of state-of-the-art methods for nanoparticle synthesis such as the hot-injection technique[13] to produce nanoparticles that are stabilized by short chain alkyl ligands having coordinatively binding groups such as phosphines, carboxylic acids, or amines. In the ligand exchange procedure these ligands are replaced by polymer chains having the same end groups to obtain nanoparticles coated with polymer chains, which are bound to the nanoparticle surface with their chain ends to form a spherical polymer brush. By varying the surface density and length of the

[a]*Universität Bayreuth, Universitätsstrasse 30, Bayreuth, Germany. E-mail: sara.mehdizadeh.taheri@uni-bayreuth.de; stephan.foerster@uni-bayreuth.de; Fax: +49 921-55-2780; Tel: +49 921-55-3924*
[b]*HASYLAB at DESY, Notkestrasse 85, Hamburg, Germany. E-mail: stephan.roth@desy.de; jan.perlich@desy.de; Fax: +49 40 8994 2934; Tel: +49 40 8998 2934*

† Electronic supplementary information (ESI) available: TEM, TGA, SAXS results. See DOI: 10.1039/c2sm26777b

polymer chains, nanoparticles with polymer layers of adjustable density and thickness can be prepared. This procedure is very versatile and can be used to coat different types of nanoparticles (Fe_2O_3, CdSe, PbS, ZnO, Au, Ag) with various types of polymers (polystyrene, polyisoprene, polyethylene oxide, polyethylene).[12] We could show that for high surface densities, the nanoparticles are very well stabilized in solution.[14]

These polymer-coated nanoparticles have a well-defined core–shell structure, the core being the nanoparticle and the shell being the solvent-swollen polymer brush. This very much resembles the core–shell structure of block copolymer micelles, which have a core of insoluble polymer blocks, and a solvent-swollen shell of the soluble block. Block copolymer micelles are known to assemble into highly ordered lyotropic phases.[15,16] Therefore we expected that polymer-coated nanoparticles would assemble similarly into lyotropic phases. This would open a route to well-defined nanoparticle superlattices without relying on DNA-hybridization, but rather employing conventional polymers on a larger scale, and a large range of nanoparticle types, which has not been attempted so far.

In the present study, we investigated narrow disperse maghemite nanoparticles in the size range of 6–17 nm, which were coated with polystyrene or polyisoprene of different molecular weights. We investigated their self-assembly behaviour in toluene, a good solvent for the polymers. Using small-angle X-ray scattering, we show for the first time that polymer stabilized nanoparticles can form highly ordered lyotropic phases. As for polymer micelles, fcc and bcc-lattices are formed, depending on the concentration and nanoparticle-to-layer size ratio and thus the softness of the interaction potential. By shear orientation in a shear-cell, macroscopic, highly ordered single crystals can be obtained. Additionally, shear orientation is possible for very small sample amounts (μL) by shear-alignment on lithographically patterned microfluidic grids.

Experimental part

Nanoparticle synthesis

Iron-oxide nanoparticles were synthesized *via* thermal decomposition of an iron oleate complex, according to the procedure of Park *et al.*[13] Typically, 10–30 g of oleate were reacted to obtain 2–8 g of monodisperse maghemite nanoparticles. The nanoparticles were characterized by transmission electron microscopy (see ESI†).

Polymer ligands

Polystyrene and polyisoprene were synthesized by living anionic polymerization initiated by sec-butyl lithium in THF at −70 °C. After completion of the polymerization, the living end groups reacted either with acetic acid to obtain unfunctionalized polymer, with CO_2 to obtain polymer with a COOH-end group, or with ethylene oxide to obtain an –OH-end group. The OH-group was activated with carbonyl diimidazol (CDI) and reacted with diethylentriamin (DETA) or pentaethylenehexamin (PEHA) to obtain amino-end functionalized polymers.[11,14] Polystyrenes and polyisoprenes with COOH– and $–C_{10}H_{28}N_6$-end groups were used as stabilizing ligands. The polymers were characterized by GPC, MALDI-TOF-MS, and ^{1}H-NMR.

Attachment of polymer chains

After their synthesis, the nanoparticles are covered with a stabilizing layer of oleic acid. The oleic acid is exchanged by a layer of end functionalized polymers *via* ligand exchange. In the case of iron-oxide nanoparticles, we used PS–COOH and PS–PEHA, PI–COOH, and PI–DETA. For the ligand exchange, a solution containing an excess of PS/PI-ligands (70 mg) in THF (1 mL) is added to a solution (200 μL) of nanoparticles (20 wt%) in toluene. Free oleic acid is removed by quantitative precipitation in ethanol. The solid containing nanoparticles, excess polymer and traces of low-molecular weight ligand is then redissolved in THF and again quantitatively precipitated in ethanol. After redissolution of the solid in THF, ethanol is added dropwise to selectively precipitate the nanoparticles from the supernatant containing the free polymer. The selective precipitation for the PS-nanocomposites is repeated in heptane. The amount of attached polymer was determined by thermal gravimetric analysis (TGA) (see ESI†).

Preparation of lyotropic solutions

For the preparation of the lyotropic nanoparticle solutions, the polymer coated nanoparticles were dissolved in the calculated amount of toluene to obtain a concentration series of 10–90% w/w. From each concentration, 15 μL were transformed into a capillary tube (diameter of 1 mm), which were melted off to avoid solvent evaporation.

For shear orientation of very small volumes of lyotropic phases, lithographically patterned microfluidic channel grids were used (Fig. 5). These grids consist of parallel aligned micron-sized channels with variable width and depth. They were produced by standard soft lithographic techniques from a PDMS master, which was used as a mold for NOA81 (Norland Optical Adhesive). NOA 81 is a UV-curable adhesive and more solvent-resisting than PDMS,[17–19] especially to toluene. For the measurements, an amount of 2–5 μL of the sample was spread on the microstructured grid. The grid was taped with Kapton to prevent solvent evaporation.

Synchrotron experiments

The measurements were performed at the beamlines BW4 and P03 at HASYLAB/DESY. At BW4, the samples were measured at a wavelength of 0.138 nm and a sample-detector distance of 108 cm. The diameter of the beam was 60 μm. The scattering patterns were detected with a MAR CCD-camera. At P03, the samples were measured at a wavelength of 0.09 nm and a sample-detector- distance of 200 cm. The diameter of the beam was 10 μm. The scattering patterns were recorded with a Pilatus 300k and Pilatus 1M detector.

Scattering curves of ordered particle systems

In the following, we describe the calculation of scattering curves for isotropic systems and scattering patterns of anisotropic shear-oriented systems of nanoparticles with solvent-swollen polymer shells dispersed in a solvent. For two-phase systems consisting of particles (phase "1") with scattering length b_1 and volume fraction ϕ_1 in a solvent (phase "2") of scattering length b_2

and a volume fraction $\phi_2 = 1 - \phi_1$, separated by sharp interfaces, the scattered intensity per unit volume is given by[20,21]

$$I(\boldsymbol{q}) = (b_1 - b_2)^2 \rho_N P(q,R)[1 + \beta(q,R)(Z(\boldsymbol{q},\boldsymbol{g}) - 1)G(q,g)] \quad (1)$$

where

$$P(q,R) = \langle F^2(q,R)\rangle_R \quad (2)$$

is the particle form factor, $F(q)$ the scattering amplitude or Fourier transform of the particle form, $\rho_N = N/V$ is the number density of the particles, $Z(\boldsymbol{q})$ is the lattice factor describing the spatial distribution of the particles, $\boldsymbol{q}$ is the scattering vector, and $G(q)$ is the Debye–Waller factor. $\langle\ldots\rangle_R$ denotes the average over the distributions of radii R. The ratio $\beta(q)$ is given by

$$\beta(q,R) = \frac{\langle F(q,R)\rangle_R^{\,2}}{\langle F^2(q,R)\rangle_R} \quad (3)$$

The effect of the ratio $\beta(q,R)$ on the scattered intensity is similar to the Debye–Waller factor, resulting in a decay of the Bragg-intensities with increasing scattering vector $\boldsymbol{q}$. Eqn (1) considers the effect of the particles – *via* their first and second moment of the particle size distribution – and of the lattice – *via* the first and second moment of the distribution of lattice points – on the scattered intensity $I(\boldsymbol{q})$.

The scattering amplitude for spheres of radius R is given by

$$F(q,R) = \frac{3}{(qR)^3}(\sin(qR) - qR\cos(qR)) \quad (4)$$

For the calculation of the average over the size distribution the Schulz-Zimm distribution is used, which yields for the z-average of a function $f(q,R)$

$$\langle f(q,R)\rangle_R = \int_0^\infty f(q,R)R^m h(R)\mathrm{d}R \quad (5)$$

with

$$h(R) = \frac{(z+1)^{z+m+1}R^z}{\bar{R}^{z+m+1}\Gamma(z+m+1)}\exp\left[-(z+1)\frac{R}{\bar{R}}\right] \quad (6)$$

and $m = 6$ is the weighting factor for the radius R, the average radius $\bar{R}$, and the relative standard deviation $\sigma_R = (z+1)^{-1/2}$. The distribution is normalized such that $\int_0^\infty R^m h(R)\mathrm{d}R = 1$. The use of a Schulz-Zimm distribution has the advantage of yielding analytical expressions for $\langle P(q)\rangle$, $\langle F(q)\rangle$, and $\beta(q)$.[20]

Using the Miller indices (hkl) for a given crystal lattice plane, the lattice factor for an ideal undistorted lattice can be written as

$$Z(\boldsymbol{q},\boldsymbol{g}) = \frac{(2\pi)^3}{nv}\sum_{\substack{h,k,l=-\infty \\ (hkl)\neq(000)}}^{\infty} f_{hkl}^{\,2} L_{hkl}(\boldsymbol{q},\boldsymbol{g}_{hkl}) \quad (7)$$

where n is the number of particles per unit cell, f_{hkl} is the structure factor of the unit cell, v is the volume of the unit cell, and $L_{hkl}(\boldsymbol{q},\boldsymbol{g}_{hkl})$ is a normalized peak shape function that depends on the reciprocal lattice vectors $\boldsymbol{g}_{hkl}$. The summation is over all values of the Miller indices (hkl) except for $(hkl) = (000)$ to ensure the calculated Porod invariant is given by $(2\pi)^{-3}V\int I(q)\mathrm{d}q = Q = \phi_1(1-\phi_1)$. The Debye–Waller factor $G(q)$ is given by

$$G(q) = \exp[-\sigma_a^{\,2}\bar{a}^2q^2] \quad (8)$$

where $\bar{a}$ is the next nearest neighbour distance between adjacent particles, which for an FCC-lattice is $\bar{a} = \frac{\sqrt{2}}{2}a$ and for a BCC-lattice is given by $\bar{a} = \frac{\sqrt{3}}{2}a$. The peak shape function $L(\boldsymbol{q},\boldsymbol{g}_{hkl})$ depends on the scattering vector $\boldsymbol{q} = (q_x,q_y,q_z)$ and the reciprocal lattice vector $\boldsymbol{g}_{hkl} = (g_{x,hkl},g_{y,hkl},g_{z,hkl})$ and can be factorized into a radial part depending on the modulus of the scattering vector, $L_q(q,g_{hkl})$, and an azimuthal part depending on the deviation angle ψ with respect to the scattering vector, $L_\psi(q,g_{hkl},\psi_{hkl})$ as

$$L(\boldsymbol{q},\boldsymbol{g}_{hkl}) = L_q(q,g_{hkl})L_\psi(\boldsymbol{q},\boldsymbol{g}_{hkl},\psi_{hkl}) \quad (9)$$

This peak shape function is normalized such that

$$\int_0^\infty\int_0^\pi\int_0^{2\pi} L_q(q,g_{hkl})L_\psi(q,g_{hkl},\psi_{hkl})q^2\sin\psi\mathrm{d}\theta\mathrm{d}\psi\mathrm{d}q = 1 \quad (10)$$

with the polar angles ψ, θ. For the radial peak shape function, we use a normalized Gaussian

$$L_q(q,g_{hkl}) = \frac{2}{\pi\delta_q}\exp\left[-\frac{4(\boldsymbol{q}-\boldsymbol{g}_{hkl})^2}{\pi\delta_q^{\,2}}\right] \quad (11)$$

where δ_q is the radial peak width, which can be related to an average domain size

$$D_l = \frac{4}{\delta_q}. \quad (12)$$

For the azimuthal peak shape, we also use a Gaussian given by

$$\tilde{L}_\psi(q,g_{hkl},\psi_{hkl}) = \frac{1}{2\pi g_{hkl}^{\,2}K(a_{hkl})}\exp\left[-\frac{4\psi_{hkl}^{\,2}q^2}{\pi\delta_\psi^{\,2}}\right] \quad (13)$$

where $a_{hkl} = \frac{4g_{hkl}^2}{\pi\delta^2}$ and $K(a_{hkl})$ is a normalization function derived in ref. 21. In the isotropic limit $\lim_{a\to 0} L_\psi(q,\psi) = \frac{1}{4\pi q^2}$. The azimuthal peak width δ_ψ can be related to an azimuthal peak width or an angular spread $\Delta\theta$ *via*

$$D_\psi = \frac{4}{\delta_\psi} = \frac{2a}{\tan\Delta\theta} \quad (14)$$

In the following, we will consider bcc- and fcc-lattices, for which the structure factors are given by

$$f_{hkl} = \begin{cases} 1+\cos[\pi(h+k+l)] & \text{for bcc} \\ 1+\cos[\pi(h+k)]+\cos[\pi(h+l)]+\cos\pi[(k+l)] & \text{for fcc} \end{cases} \quad (15)$$

Fcc and bcc lattices occur in twinned configurations. The reciprocal lattice vectors $\boldsymbol{g}_{hkl} = ha^* + kb^* + lc^*$ for the corresponding twins are given in Table 1.

We have found that eqn (1) describes scattering curves and scattering patterns remarkably well for a large variety of mesoscopically ordered materials.[21] The use of closed analytical

Table 1 Reciprocal lattice vectors a^*,b^*,c^* for FCC and BCC twins. e_x, e_y, and e_z are the unit vectors of the Carthesian coordinate system

	a^*	b^*	c^*
FCC twin A	$\frac{2\pi}{a}e_x$	$\frac{2\pi}{a}e_y$	$\frac{2\pi}{a}e_z$
FCC twin B	$\frac{2\pi}{3a}(2e_x - e_y + 2e_z)$	$\frac{2\pi}{3a}(2e_x + 2e_y - e_z)$	$\frac{2\pi}{3a}(-e_x + 2e_y + 2e_z)$
BCC twin A	$\frac{2\pi}{a}e_x$	$\frac{2\pi}{a}e_y$	$\frac{2\pi}{a}e_z$
BCC twin B	$\frac{2\pi}{3a}(2e_x + e_y - 2e_z)$	$\frac{2\pi}{3a}(e_x + 2e_y + 2e_z)$	$\frac{2\pi}{3a}(2e_x - 2e_y + e_z)$

functions facilitates computing and allows efficient implementation into fitting routines. It allows to quickly extract the unit cell size a, the mean deviation from the lattice points σ_a, the nanoparticle radius R, its relative standard deviation σ_R (polydispersity), and the mean size of the crystalline domains D from measured scattering curves and scattering patterns. Eqn (1) also reproduces correctly secondary Bragg-peaks that appear as a consequence of the finite peak width as outlined in ref. 21. An executable version of the software (Scatter)[22] can be obtained from the author.

Results and discussion

Isotropic concentration series

Fig. 1 shows measured synchrotron-SAXS curves of a concentration series of Fe_2O_3 (6 nm)@PS–COOH(8k) nanoparticles in toluene. At the lowest concentrations we observe a broad maximum at $q \sim 0.3$ nm^{-1} indicating weak positional correlations between the nanoparticles. The minimum at $q = 1.4$ nm^{-1} corresponds to the sphere form factor minimum, from which the radius of the nanoparticles can be estimated to be 6.1 nm, in good agreement with the TEM measurements. With increasing concentration, the maximum becomes more pronounced and shifts to larger q-values. Between a concentration of 60 and 70 wt%, we observe a disorder–order transition, indicated by the sharp Lorentzian-type shape of the first-order peak and the appearance of higher order reflections.

The peak positions can be indexed on a bcc-lattice (space group *Im*3*m*). Also in the dry state we observe the formation of a bcc-lattice. The lattice order is well comparable to micellar lyotropic phases in water. The form factor minimum does not vanish or shift, indicating that the polymer-stabilized nanoparticles show no aggregation, even for the highest concentrations and in bulk.

The measured scattering curves can be quantitatively described by eqn (1) to obtain more detailed structural information. From the analysis we directly obtain the unit cell dimension, the mean displacement of the nanoparticles from the lattice points, the nanoparticle radius with the relative standard deviation (particle polydispersity), as well as the mean size of the crystalline domains. All values are summarized in Table S2 in the ESI.† The observed values are all typical for lyotropic phases. The unit cell sizes decrease with increasing concentration from 28–15 nm, the mean deviation from the lattice points is 2.1 nm (12% relative to the unit cell size) and the domain sizes increase with increasing concentration from 30–97 nm. The radius of the nanoparticles is 6.1 nm with a polydispersity of 9.5%.

Fig. 2 shows measured synchrotron-SAXS curves of a concentration series of Fe_2O_3 (17 nm)@PS–N_6(28k) nanoparticles in toluene. Since the nanoparticles are larger, we observe more form factor oscillation in the measured q-range, with the first minimum at $q \sim 0.55$ nm^{-1}. Also for this case we did not observe shifts or damping of the form factor oscillations which would indicate nanoparticle aggregation, even at the highest concentrations and in the solid state. Since the attached polymer chains are larger, we observe the disorder–order transition at lower concentrations, *i.e.* between 30 and 40 wt%. Then with increasing concentration the nanoparticles first form an

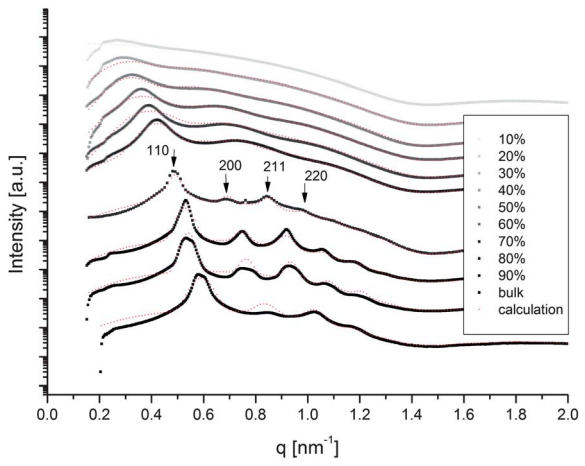

Fig. 1 Synchrotron SAXS-curves measured at BW4/DESY for Fe_2O_3 (6 nm)@PS–COOH(8k) at different concentrations in toluene. At a concentration between 60 and 70%, we observe a disorder–order transition into a bcc-phase. The dotted lines indicate fits to the measured scattering curves using eqn (1).

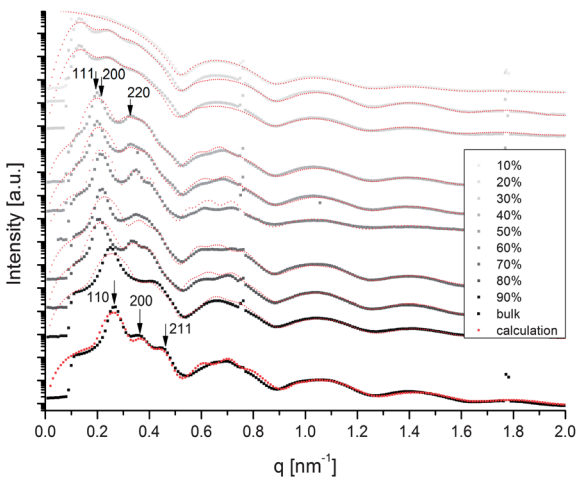

Fig. 2 Synchrotron SAXS-curves measured at BW4/DESY for Fe_2O_3 (17 nm)@PS–N_6(28k) at different concentrations in toluene. At a concentration between 30 and 40% we observe a disorder–order transition into an fcc-phase, and at 70% into a bcc-phase. The dotted lines indicate fits to the measured scattering curves using eqn (1).

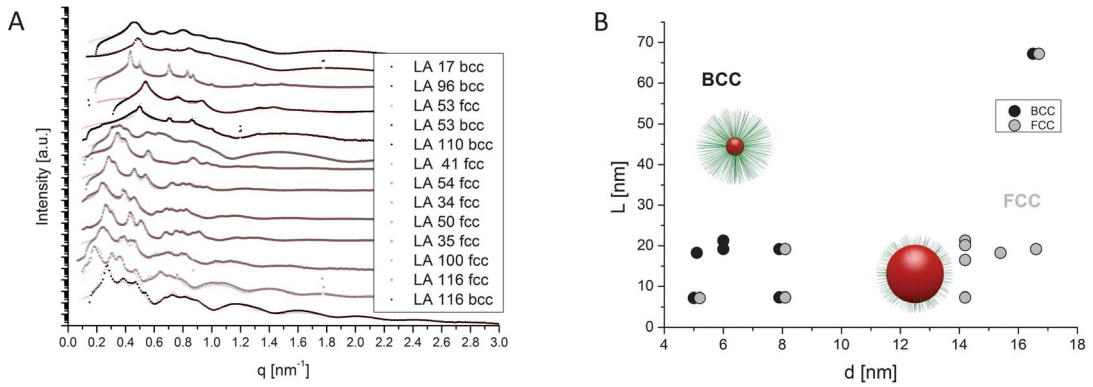

Fig. 3 (A) Synchrotron SAXS-curves measured at BW4/DESY for different nanoparticle/polymer-systems in toluene in the ordered lyotropic state. The sample codes are related to the nanoparticle diameters and polymer molecular weights in Table 2. (B) Stability regions of bcc- and fcc-phases as a function of nanoparticle diameter and polymer contour length.

fcc-structure (*Fm*3*m*) and at 70 wt% they show a phase transition to a bcc structure (*Im*3*m*). For the bulk sample the bcc unit cell size is 33 nm. Also this set of scattering curves could be fit quantitatively to eqn (1) to obtain structural details of the lyotropic phases. The unit cell sizes decrease with increasing concentration from 54–45 nm for fcc, and then from 40–35 nm for the bcc-lattices. The mean deviation from the lattice points is 2.6 nm (12% relative to the unit cell size) and the domain sizes are in the range of 300–400 nm. The radius of the nanoparticles is 17.1 nm with a polydispersity of 7.5%.

Using synchrotron-SAXS we have investigated many more nanoparticle/polymer lyotropic phases at different concentrations with different nanoparticle sizes (5–17 nm) and attached polymer molecular weights (2000–28 000 g mol^{-1}). The measured scattering curves are shown in Fig. 3A. Results of the fits to the scattering curves are all summarized in Table S3 in the ESI.† With increasing concentration up to the bulk nanoparticle/polymer nanocomposite we observe two typical lyotropic phase sequences DIS → FCC → BCC or DIS → BCC, depending on the nanoparticle size and attached polymer chain molecular weight.

From our investigations, we can give a schematic overview for the stability ranges for bcc- and fcc-structures, which appears to depend on the ratio of nanoparticle radius to attached polymer molecular weight. To compare the effect of different molecular weights of polystyrene and polyisoprene, we related the molecular weights to the contour lengths of the polymer chains, assuming a contour length of 0.25 nm for the monomers. The values are given in Table 2. In Fig. 3B, we have plotted a diagram displaying the observed lyotropic phase structure as a function of nanoparticle size and polymer contour length. We observe that systems consisting of small nanoparticles (5–8 nm) with long polymer chains (18–22 nm) prefer bcc-packing, whereas larger nanoparticles (14–17 nm) with attached polymer chains in the contour length range of 7–21 nm prefer fcc-packing. For the largest nanoparticle (17 nm) with the longest polymer chains (67 nm), we observe a fcc/bcc-coexistence. In the schematic representation in Fig. 3B we observe bcc phases in the upper left and fcc in the lower right, with a coexistence region in between. The scheme in Fig. 3B is not meant as a phase diagram, but merely to display the observed trend. For large polymer chains attached to small nanoparticles, where mainly bcc-structures are observed, we have a strongly curved spherical polymer brush structure with low segment densities at the layer periphery. These would mediate very soft interactions. For shorter polymer chains attached to larger nanoparticles, we have less curved spherical polymer brush structures with dense layers and higher segment density at the periphery, which is expected to mediate harder interactions. The observation of bcc-structures for soft interacting colloids and fcc-structures for colloids with harder interactions is similarly observed for block copolymer micelles as shown by Gast.[23] In the solid state, bcc is always stable, analogous to block copolymer melts.

Shear-oriented lyotropic phases

As for block copolymer melts or block copolymer lyotropic phases, we found it to be possible to shear-orient lyotropic nanoparticle phases to obtain for the first time macroscopically oriented single crystalline nanoparticle superlattices. Shear-orientation was performed in a plate–plate shear cell (Linkam) with a gap size of 100 μm. We found that oscillatory shear at frequencies of 1–10 s^{-1} and shear amplitudes of 5–10 for 10 s

Table 2 Sample codes, polymer types (PS = polystyrene, PI = polyisoprene), lattice type of the lyotropic phase, polymer molecular weight, contour length, and nanoparticle diameters for the nanocomposites measured in Fig. 3A

Sample	LA 17 (PI)	LA 96 (PS)	LA 53 (PI)	LA 110 (PS)	LA 41 (PS)	LA 54 (PI)	LA 34 (PI)	LA 50 (PI)	LA 35 (PS)	LA 100 (PS)	LA 116 (PS)
Lattice	Bcc	Bcc	Fcc/Bcc	Bcc	Fcc	Fcc	Fcc	Fcc	Fcc	Fcc	Fcc/Bcc
Polymer [g mol^{-1}]	5800	8000	2000	8000	8000	2000	4500	5800	8400	8000	28 000
Contour length [nm]	21.3	19.2	7.3	19.2	19.2	7.3	16.5	21.3	20.1	19.2	67.2
Nanoparticle diameter [nm]	6	6	8	8	8	14.2	14.2	14.2	14.2	16.6	16.6

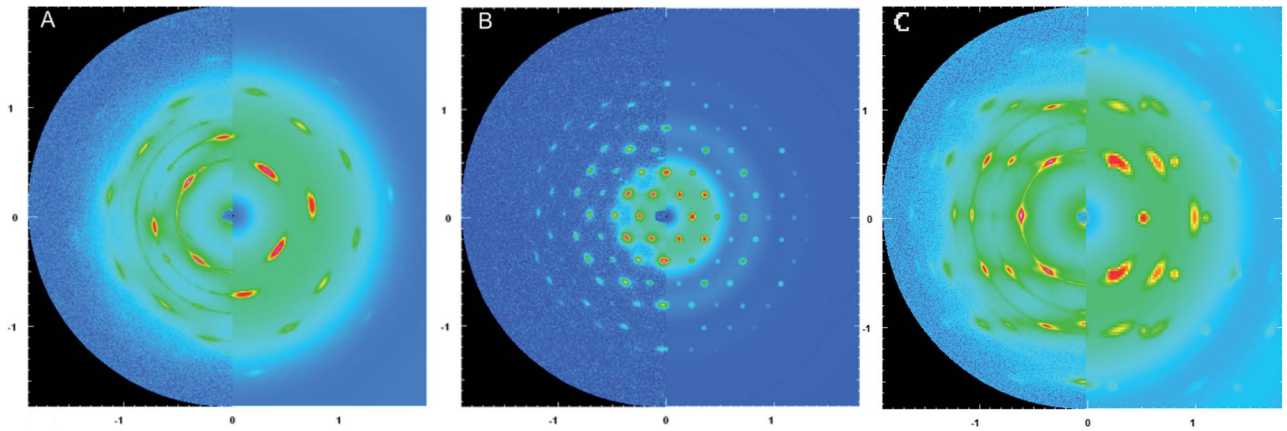

Fig. 4 Scattering patterns of shear-oriented lyotropic phases of Fe_2O_3 (5.1 nm)@PS–DETA(7.6k) forming a bcc-structure (A), Fe_2O_3 (15.4 nm)@PS–DETA(7.6k) forming a fcc-structure (B), and Fe_2O_3 (5.1 nm)@PS–DETA(3k) (C) showing a coexistence of bcc and fcc structures measured at BW4/DESY. Measurements are shown on the left halves, and calculations using eqn (1) are shown on the right halves of the patterns.

were suitable conditions for shear-alignment. The measured scattering patterns for different nanoparticle/polymer lyotropic phases are shown in Fig. 4. We observe a large number (>100 in Fig. 4B) of Bragg-reflections, indicating a high degree of lyotropic crystalline order. Indexing of these reflections is only possible by taking into account secondary Bragg-peaks which are observable as a consequence of the large peak widths typical for lyotropic crystals as outlined in ref. 24.

For Fe_2O_3 (5.1 nm)@PS–DETA(7.6k) (Fig. 4A), which was shear-oriented at 4 Hz and a shear amplitude of 9, we observe a bcc-structure oriented such that the [110]-direction is parallel to the X-ray beam and the [1$\bar{1}$2]-direction is oriented in the shear direction. This shear-alignment structure is typical for colloidal lyotropic crystals. The alignment orients the line of highest particle density [1$\bar{1}$2] parallel to the flow-direction and the plane of highest particle density (110) normal to the gradient direction, which is parallel to the X-ray beam. Bcc occurs in a twinned configuration. The twins both align with their [1$\bar{1}$2]-direction in the shear direction, with the (1$\bar{1}$2)-plane being the mirror plane that relates each of the twins.[24] The scattering pattern can be quantitatively analyzed by eqn (1). The calculated scattering pattern is merged into the measured scattering pattern to show remarkably good agreement. The structural parameters derived from the calculation such as unit cell dimension, mean deviation from the lattice points, domain size, particle size and its mean square deviation are given in Table 3. The nearest neighbour distance between adjacent nanoparticles is 15 nm, which is considerably larger compared to the 8.8 nm observed for the bulk phase. We observe that both twin structures occur with equal probability.

For Fe_2O_3 (15.4 nm)@PS–DETA(7.6k) (Fig. 4B), which was shear-oriented at 8 Hz and an amplitude of 9, we observe a fcc-structure. It orients such that the line of highest particle density [$\bar{1}$10] is parallel to the flow direction and the plane of highest particle density [111] orients normal to the gradient direction, parallel to the X-ray beam. Also in this case, eqn (1) very well describes the scattering pattern. The calculated scattering pattern is merged into the measured scattering pattern to show excellent agreement. It is worth mentioning that nearly 2/3 of the more than 100 observed peaks are secondary Bragg reflections due to finite peak widths, which would usually be considered crystallographically forbidden. Also for this calculation, the structural parameters are given in Table 3. The nearest neighbour distance is 31 nm which can be compared to the bulk value of 21 nm.

A complex and very interesting scattering pattern is shown in Fig. 4C. This scattering pattern was measured for Fe_2O_3 (5.1 nm)

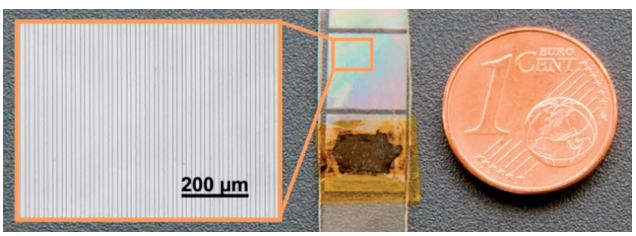

Fig. 5 Micro structured NOA 81 array with 1 cm × 1 cm patches consisting of 14 µm channel grids, used to spread and shear-orient very small sample amounts (2–5 µL) of lyotropic phases. The lower patch has been filled with a nanoparticle lyotropic gel and sealed with Kapton tape to avoid solvent evaporation during X-ray measurements.

Table 3 Calculated structural information for measured 2D-SAXS pattern

Sample	Lattice	q_x	q_y	q_z	Unit cell [nm]	Mean displacement [nm]	Radial domain size [nm]	Azimuthal domain size [nm]
Fe_2O_3 (5.1 nm)@PS–DETA(7.6k)	BCC	1$\bar{1}$1	$\bar{1}$1$\bar{2}$	110	17.0	2.0	180	50
Fe_2O_3 (15.4 nm)@PS–DETA(7.6k)	FCC	1$\bar{1}$2	1$\bar{1}$0	111	44.0	2.8	200	50
Fe_2O_3 (5.1 nm)@PS–DETA(3k)	BCC	1$\bar{1}$1	$\bar{1}$1$\bar{2}$	110	14.0	1.0	100	10
	FCC	1$\bar{1}$2	1$\bar{1}$0	111	17.0	1.0	100	35

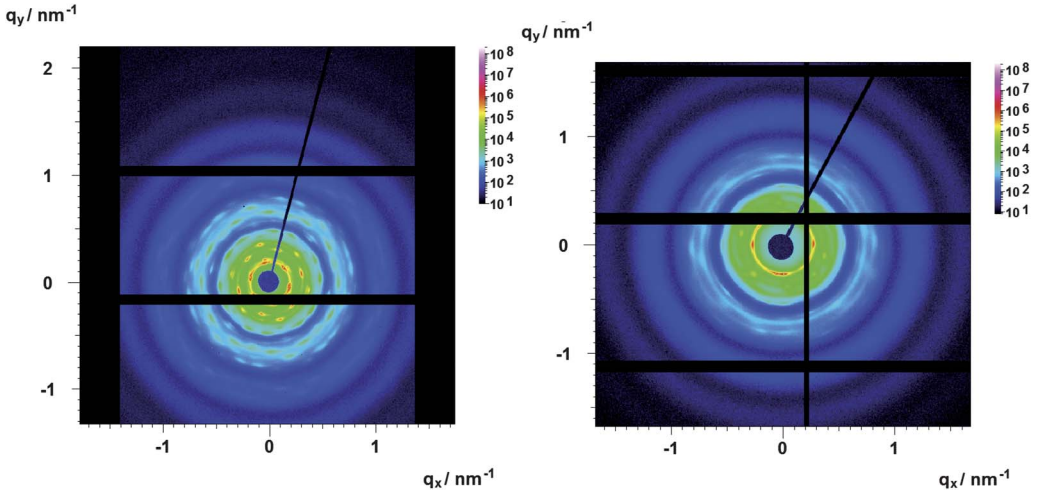

Fig. 6 SAXS-patterns measured with a microfocused X-ray beam at P03/DESY for Fe_2O_3 (16.6 nm)@PS–DETA(28k) at a concentration of 50%wt (fcc) (A) and 70%wt (bcc) (B). The samples were oriented in a specially designed microchannel sample holder where sample amounts of only 2–5μL are needed.

@PS–DETA(3k). The sample could only be oriented by applying continuous shear at a shear rate of 750 s^{-1}. The pattern has similarities to the patterns observed for the bcc and fcc-structures and corresponds to a coexistence of both phases. Assuming both structures to be aligned as in Fig. 4A and B, then all peaks can be appropriately indexed and even a quantitative calculation is possible that is merged into the experimentally determined scattering pattern. It gives very good agreement and yields a relative composition fcc–bcc of 0.7 : 0.3.

An interesting point is that in coexistence there should be an epitaxial relation with respect to both the unit cell dimensions and orientations. The phase transition is believed to proceed *via* slight rearrangements of the particles within the unit cells *via* a tretragonal transition state (Bain transition) similar to the Martensitic transition in steel. If this is the case, then the 111-reflection for fcc and the 110-reflection for bcc should appear at the same position. Assuming the volume fraction ϕ is constant upon this transition, then the unit cell dimensions should be related as $a_{fcc} = 2^{1/3} a_{bcc} \approx 1.26 a_{bcc}$, which is experimentally well fulfilled as $a_{fcc}/a_{bcc} = 17/14 = 1.22$ (see Table 3).

Also the phase structures for the shear-oriented nanoparticle lyotropic phases are included in the Scheme in Fig. 3B and fit well into the trend that small nanoparticles (5.1 nm) with large polymer chains (7.6 k) form bcc structures (Fig. 4A), larger nanoparticles (15.4 nm) form fcc structure with the same polymer (7.6 k) (Fig. 4B), and small nanoparticles (5.1 nm) with shorter polymer chains (3 k) show a tendency toward fcc structures, leading to the observed bcc/fcc-coexistence (Fig. 4C).

Shear-orientation in micro structured grids

For shear orientation in conventional shear cells (Couette, Searle, plate–plate), at least 1–5 mL of the sample is usually required, which is often more than can be produced when dealing with valuable materials such as nanoparticles, proteins or DNA. This motivated us to prepare micro sample holders which allowed shear orientation of very small amounts of gel-like samples. In an analogous fashion to the production of microchannels for microfluidic chips, we used soft lithography to prepare sample holders with linear arrays of 1 cm × 1 cm patches, each consisting of 10–100 parallel aligned microchannels with diameters between 10 and 100 μm and a depth of 300 μm.

Fig. 5 shows an example of a linear array of patches consisting of 14 μm width channels. The sample holder is produced in NOA 81 (Norland Optical Adhesive), which can be produced by conventional soft lithography, is resistant against a large variety of solvents, including water and toluene, and is X-ray transparent, mechanically stable and amorphous with very little X-ray background. By spreading a gel-like sample into a microchannel patch, the shear force orients the liquid crystalline structure. For the microstructured channel device shown in Fig. 5, only 2–5 μL of the sample is needed. The microchannel patch can be sealed with conventional Kapton tape to avoid solvent evaporation. Fig. 6 shows the scattering patterns measured for the sample Fe_2O_3 (16.6 nm)@PS–DETA(28k). We observe the typical 111-orientation of the shear-oriented fcc-phase at lower concentrations (Fig. 6A) and the transition into the bcc-phase at higher concentrations (Fig. 6B).

Conclusions

We show that polymer-coated nanoparticles can form liquid crystalline lyotropic phases with high order very similar to micellar lyotropic liquid crystals of surfactants and polymers. We observe the formation of bcc and fcc phases with a trend that small nanoparticle/large polymer systems form bcc-structures, and large nanoparticle/small polymer systems form fcc-structures. This appears to be a consequence of the softness of the polymer layers and the segment density at the periphery of the layer and is very similar to observations of block copolymer micelles in solution and bulk. Within the ordered phases, the distance between adjacent nanoparticles can be varied systematically *via* concentration and attached polymer molecular weights in a range of 10–40 nm. It is possible to shear-orient the nanoparticle lyotropic phases to obtain for the first time

macroscopically oriented highly ordered nanoparticle superlattice single crystals. In addition, we present microstructured sample holders that allow shear orientation and investigations of very small sample amounts (μL) of lyotropic phases.

Notes and references

1 C. B. Murray, C. R. Kagan and M. G. Bawendi, *Science*, 2008, **270**, 1335.
2 D. V. Talapin, J.-S. Lee, M. V. Kovalenko and E. V. Shevchenko, *Chem. Rev.*, 2010, **110**, 389.
3 S. M. Taheri, S. Fischer and S. Förster, *Polymer*, 2011, **3**, 662.
4 E. V. Shevchenko, D. V. Talapin, A. Kornowski, F. Wiekhorst, J. Kötzler, M. Haase, A. L. Rogach and H. Weller, *Adv. Mater*, 2002, **14**, 287.
5 J. E. Martin, J. P. Wilcoxon, J. Odinek and P. Provencio, *J. Phys. Chem. B*, 2000, **104**, 9475.
6 A. P. Alivisatos, K. P. Johnsson, X. Peng, T. E. Wilson, C. J. Loweth, M. P. Bruchez, Jr and P. G. Schultz, *Nature*, 1996, **382**, 609.
7 C. A. Mirkin, R. L. Letsinger, R. C. Mucic and J. J. Storhoff, *Nature*, 1996, **382**, 607.
8 R. J. Macfarlane, M. R. Jones, A. J. Senesi, K. L. Young, B. Lee, J. Wu and C. A. Mirkin, *Angew. Chem., Int. Ed.*, 2010, **49**, 4589.
9 W. Cheng, M. J. Campolongo, J. J. Cha, S. J. Tan, C. C. Umbach, D. A. Muller and D. Luo, *Nat. Mater.*, 2009, **8**, 519.
10 W. Cheng, M. R. Hartman, D.-M. Smilgies, R. Long, M. J. Campolongo, R. Li, K. Sekar, C.-Y. Hui and D. Luo, *Angew. Chem., Int. Ed.*, 2010, **49**, 380.
11 M. A. Nikolic, V. Alexandrovic, M. Krack, A. Kornowski, S. Förster and H. Weller, *Angew. Chem., Int. Ed.*, 2006, **45**, 6577.
12 S. Fischer, A. Salcher, A. Kornowski, H. Weller and S. Förster, *Angew. Chem., Int. Ed.*, 2011, **123**, 7957.
13 J. Park, K. An, Y. Hwang, J.-G. Park, H.-J. Noh, J.-Y. Kim, J.-H. Park, N.-M. Hwang and T. Hyeon, *Nat. Mater.*, 2004, **3**, 891.
14 M. S. Nikolic, A. Kornowski, A. Rank, R. Schubert, A. Frömsdorf, H. Weller and S. Förster, *Angew. Chem., Int. Ed.*, 2009, **48**, 2619.
15 H.-P. Hentze, E. Krämer, B. Berton, D. Förster and M. Antonietti, *Macromolecules*, 2000, **35**, 3523.
16 S. Förster and T. Plantenberg, *Angew. Chem., Int. Ed.*, 2002, **41**, 688.
17 D. Bartolo, G. Degré, P. Nghe and V. Studer, *Lab Chip*, 2008, **8**, 274.
18 L.-H. Hung, R. Lin and A. P. Lee, *Lab Chip*, 2008, **8**, 983.
19 Ph. Wägli, B. Y. Guélat, A. Homsy and N. F. Rooij, *14th International Conference on Miniaturized Systems for Chemistry and Life Sciences*, 2010, p. 1937.
20 S. Förster, A. Timmann, M. Konrad, C. Schellbach, A. Meyer, S. S. Funari, P. Mulvaney and R. Knott, *J. Phys. Chem. B*, 2005, **109**, 1347.
21 S. Förster, S. Fischer, K. Zielske, C. Schellbach, M. Sztucki, P. Lindner and J. Perlich, *Adv. Colloid Interface Sci.*, 2011, **163**, 53.
22 S. Förster, L. Apostol and W. Bras, *J. Appl. Crystallogr.*, 2010, **43**, 639.
23 G. A. McConnell, A. P. Gast, J. S. Huang and S. D. Smith, *Phys. Rev. Lett.*, 1993, **71**, 2102.
24 S. Förster, A. Timmann, C. Schellbach, A. Frömsdorf, A. Kornowski, H. Weller, S. V. Roth and P. Lindner, *Nat. Mater.*, 2007, **6**, 888.